Bioactive Materials 44 (2025) 269–282

Contents lists available at ScienceDirect

Bioactive Materials

journal homepage: www.keaipublishing.com/en/journals/bioactive-materials

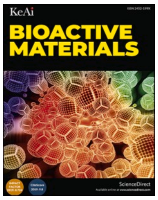

Acid-responsive CST@NPs enhanced diabetic wound healing through rescuing mitochondrial dysfunction

Xuelian Zhang [a,1], Hang Li [b,1], Yang Liu [c,1], Jie Yu [d,1], Pengfei Zhang [b], Peiling Yu [e], Yuhao Liu [b], Suyi Jia [f], Lijuan Ling [g], Peng Li [b], Lei Li [b], Yueyao Wang [e], Tengxiao Huang [b], Gaoxin Jin [f], Yunpeng Zhao [b], Guoli Ma [b], Qinghao Yuan [f], Lei Zhu [b,****], Zhiyue Zhang [c,***], Hao Li [b,**], Weiwei Li [e,*]

[a] *Department of Endocrinology, China-Japan Friendship Hospital, Beijing, 100029, PR China*
[b] *Department of Orthopaedic Surgery, Qilu Hospital, Cheeloo College of Medicine, Shandong University, Jinan, 250012, PR China*
[c] *NMPA Key Laboratory for Technology Research and Evaluation of Drug Products, Key Laboratory of Chemical Biology (Ministry of Education), Shandong Key Laboratory of Targeted Drug Delivery and Advanced Pharmaceutics, Department of Pharmaceutics, School of Pharmaceutical Sciences, Cheeloo College of Medicine, Shandong University, Jinan, Shandong, 250012, PR China*
[d] *Department of Radiology, Qilu Hospital, Cheeloo College of Medicine, Shandong University, Jinan, 250012, PR China*
[e] *Department of Pathology, Qilu Hospital, Cheeloo College of Medicine, Shandong University, Jinan, 250012, PR China*
[f] *Cheeloo College of Medicine, Shandong University, Jinan, Shandong, 250012, PR China*
[g] *Chinese People's Liberation Army General Hospital, JingZhong MED, Huangsi Out-patient Department, Beijing, 100120, PR China*

ARTICLE INFO

Keywords:
Diabetic wound healing, Cortistatin
Nanoparticle
Acid-responsive
Mitochondria
Apoptosis

ABSTRACT

Diabetic ulcers (DUs) are persistent and challenging complications of diabetes. The consequences of DUs include a decline in functional status, increased risk of infection, hospitalization, and even death. Our study revealed a significant decrease in the levels of cortistatin (CST) in the skin tissue of patients with DUs and diabetic rats. This finding led us to hypothesize that the administration of exogenous CST is an effective strategy to promote wound healing in patients with DUs. We herein successfully prepared CST-loaded pDMA-pEPEMA nanoparticles (CST@NPs) designed to exhibit localized, acid-responsive behavior for enhanced wound healing. These CST@NPs were sensitive to acidic environments, triggering the rapid release of CST. *In vitro* experiments showed that CST@NPs effectively alleviated oxidative stress and reduced apoptosis in human umbilical vein endothelial cells (HUVECs). Our findings further demonstrated that CST@NPs accelerated re-epithelialization of the wound, enhanced collagen deposition, and stimulated angiogenesis, while alleviating the local inflammatory response. Both *in vivo* and *in vitro* results indicate that CST@NPs possess precise and rapid response capabilities in acidic environments, ensuring effective CST release to promote diabetic wound healing. In summary, this acid-responsive nanoparticle system presents a highly efficient therapeutic strategy for the treatment of chronic diabetic wounds.

1. Introduction

At present, the treatment of diabetic ulcers (DUs)—a serious and multifaceted complication of diabetes—faces significant challenges and shows an alarmingly high rate of disability. DUs are characterized by very difficult wound healing due to drug-resistant bacterial infections, reduced angiogenesis, and oxidative damage in the microenvironment [1,2]. In diabetic conditions, the wound healing process stalls during the

---

Peer review under responsibility of KeAi Communications Co., Ltd.

* Corresponding authors.
** Corresponding author.
*** Corresponding authors.
**** Corresponding author.
E-mail addresses: zhuleijn@aliyun.com (L. Zhu), zhiyue.zhang@sdu.edu.cn (Z. Zhang), hal@email.sdu.edu.cn (H. Li), liweiwei@qiluhospital.com (W. Li).

[1] These authors contribute equally.

https://doi.org/10.1016/j.bioactmat.2024.10.004
Received 1 July 2024; Received in revised form 30 September 2024; Accepted 2 October 2024

inflammatory phase due to a persistent inflammatory environment that triggers an overproduction of reactive oxygen species (ROS) which exceeds cellular self-antioxidant defenses, leading to a state of oxidative stress that fuels inflammation and disrupts mitochondrial redox homeostasis [3–6], resulting in widespread mitochondrial dysfunction and a subsequent bioenergetic imbalance, which is suggested to play a key role in cellular anabolism during cell differentiation and proliferation. Thus, the restoration of mitochondrial functions has been identified as a potential target for promoting tissue regeneration in diabetic wounds [7] (see Scheme 1).

Cortistatin (CST) is a peptide hormone isolated from the cerebral cortex and peripheral tissues, including the immune system, gastrointestinal tract, and endocrine pancreas. CST is explicitly expressed in immune cells, appears to be involved in monocyte differentiation, and is considered a potent anti-inflammatory agent that lessens the inflammatory response *in vivo* [8]. CST deficiency has recently been associated with the development of inflammatory bowel disease, pulmonary fibrosis, immune myocarditis, and other diseases [9–11]. In our previous studies, we demonstrated that CST deficiency leads to various inflammatory conditions, including osteoarthritis, disc degeneration, and immune-related abnormalities such as psoriasis [12–14]. Our latest study reveals significant downregulation of gene expression associated with mitochondrial function in CST$^{-/-}$ mice, suggesting a potential association between chronic healing of diabetic wounds and CST deficiency. Our study also revealed a significant reduction in CST expression in the skin of patients with diabetes. This evidence suggests that mitochondrial dysfunction caused by CST deficiency is closely related to chronic healing of diabetic wounds.

Nonetheless, the application of simple peptides alone has some limitations. Their susceptibility to protease degradation, poor stability, short duration of drug action, and the need for frequent administration impose a significant physiological and psychological burden on patients. Therefore, improving the stability of protein and peptide drugs *in vivo* is crucial [15–17]. Considering the local acidic microenvironment of diabetic wounds and the potential anti-inflammatory properties of CST, it is essential to develop a biomaterial that can induce a local acidic response, improve CST stability, and achieve sustained CST release for effective diabetic wound treatment.

Nanoparticles (NPs) have many notable advantages over conventional drug delivery systems: (1) NPs demonstrate minimal toxicity, ensuring their compatibility with skin and creating an ideal moist environment to activate and expedite wound healing. (2) Specific nanoparticles can penetrate cellular barriers and access cytoplasmic spaces or trigger targeted transport mechanisms, enhancing drug retention and efficacy. (3) Combining nanoparticles with bioactive molecules can protect drugs from protease degradation at the wound site, significantly improving their therapeutic impact. (4) Controlled drug release extends the duration of effective drug concentrations, reducing side effects, minimizing the frequency of administration and associated costs, and enhancing patient adherence [2,18–22].

Diabetic wounds have an extremely complex microenvironment of hyperglycemia, acidity and high reactive oxygen species (ROS) [23]. Based on the above extremely complex microenvironment, microenvironment-active materials or delivery systems can be designed and fabricated to improve the therapeutic effect [24,25]. In this study, acid-responsive drug delivery nanoparticles CST@NPs were prepared based on the acidic environment of wound surface. Accordingly, designing nanoparticles with pH-responsiveness and controlled drug release functions is an exceptional strategy for treating DU wounds. The protonation of EPEMA in amphiphilic polymers pDMA-pEPEMA in an acidic environment allows the responsive release of CST. These nano-delivery systems enable continuous and long-term administration of loaded drugs to acidic target sites [26]. pDMA-pEPEMA offers superior drug-carrying capacity, better stability, lower dosing frequency, and versatility in administration methods than other polymers.

Therefore, we prepared CST-loaded pDMA-pEPEMA NPs (CST@NPs) to improve the pharmacokinetic profile of CST, enhancing the microvascular environment in diabetes [27]. This novel acid-responsive nanomedicine has shown remarkable anti-inflammatory, anti-oxidative, anti-apoptotic, and pro-angiogenic properties. We also evaluated the effect of CST@NPs at different stages of DU healing in low-dose streptozotocin-induced diabetic rats and mice [28–30]. *In*

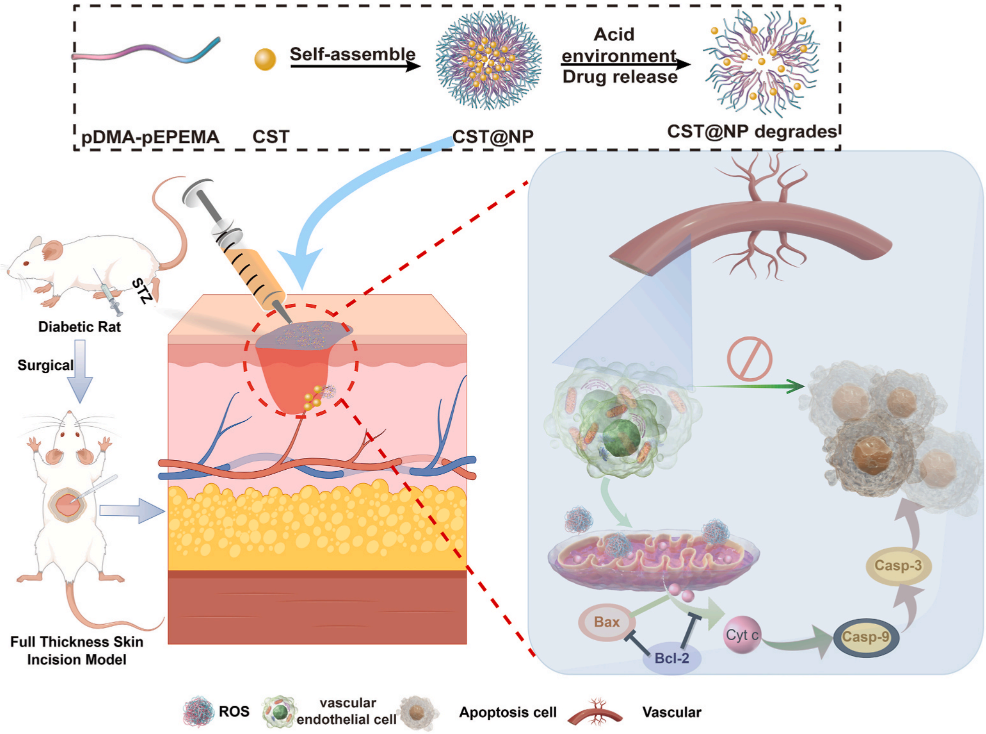

Scheme 1. Schematic diagram of the construction of acid-responsive CST@NPs and cascade reaction for the mechanism of diabetic wound healing (By Figdraw).

vitro studies revealed that CST effectively promotes wound healing by suppressing inflammatory response and facilitating angiogenesis. These advantages make CST@NPs a highly promising treatment approach for diabetic wounds characterized by delayed healing [31,32].

Our findings provide a theoretical foundation and a novel approach for progressing the development of nano-delivery systems in the treatment of DUs.

2. Experimental section/methods

2.1. Characterizations

2.1.1. Materials

N-ethyl ethanolamine was purchased from Bide Pharmaceuticals. Bromopropane, methacryloyl chloride, and triethylamine were obtained from Energy Chemical. 4-cyano-4-(dodecylsulfanylthiocarbonyl) sulfanyl pentanoic acid and 1,4-dioxane were sourced from Aladdin Reagent Co., Ltd.

2.1.2. Synthesis of EPEMA

EPEMA was synthesized in two steps. The first step: N-ethyl ethanolamine (0.30 mol), bromopropane (0.45 mol) and Na_2CO_3 (0.50 mol) were added to a round-bottomed flask and dissolved in acetonitrile (100 mL). The above mixture was stirred continuously at 80 °C for 24 h. At the end of the reaction, the mixture solution was filtered, and the filtrate was taken and dried to get the crude product. Then, the crude product was redissolved with DCM and washed with MiliQ for 3 times. Finally, the DCM phases were collected and dried to obtain the product.

The second step: The product synthesized in the first step (22.50 mmol) and triethylamine (TEA) (40.00 mmol) were added to a round-bottom flask and dissolved with acetonitrile. The above mixture was stirred in ice bath, and then the methacryloyl chloride (32.50 mmol) was added and stirred continuously for 2 h, followed by stirring at room temperature for 12 h. At the end of the reaction, the mixture solution was filtered, and the filtrate was taken and dried to get the crude product. Then, the crude product was redissolved with DCM and washed with MiliQ for 3 times. Finally, the DCM phases were collected and dried to obtain the EPEMA. The structure of EPEMA was verified by ^1H nuclear magnetic resonance (^1H NMR).

2.1.3. Synthesis of pDMA

The hydrophilic homopolymer pDMA was prepared by reversible addition-fragmentation chain transfer (RAFT) polymerization. DMA (20 mmol), 4-cyano-4-(dodecylsulfanylthiocar-bonyl) sulfanyl pentanoic acid (DCT) (0.4 mmol) and 2,2′ -azobis (2-methylpropionitrile) (AIBN) (0.08 mmol) were dissolved in 1,4-dioxane and transferred to a 25 mL Schlenk tube. The oxygen was removed through three freeze-thaw cycles, and the reaction was carried out in oil bath at 80 °C for 4 h. The reaction solution was precipitated three times in a mixture of diethyl ether and hexane and dried under vacuum to obtain the yellow product pDMA. The successful polymerization of pDMA was verified by ^1H NMR.

2.1.4. Synthesis of pDMA-pEPEMA

The amphiphilic and acid-responsive homopolymer pDMA-pEPEMA was similarly prepared by RAFT polymerization. pDMA (0.05 mmol), EPEMA (2.5 mmol) and AIBN (0.015 mmol) were dissolved in 1,4-dioxane and transferred to a 25 mL Schlenk tube. The oxygen was removed through three freeze-thaw cycles, and the reaction was carried out in oil bath at 80 °C for 24 h. Finally, the final polymer pDMA-pEPEMA was obtained by dialysis in water and freeze-dried. The monomer conversion rate was verified by ^1H NMR.

2.1.5. Preparation of CST-loaded and acid-responsive nanoparticles

CST@NPs was prepared by the nanoprecipitation method. The method was described as follows: CST and pDMA-pEPEMA were dissolved in pH 5.0 PBS or DMSO. Then, the CST@NPs were prepared by dropping the above mixed solution into pH 7.4 PBS (containing 1 % Tween) under ultrasound and continuous ultrasound for 30 min.

2.1.6. Characterization of CST@NPs

The particle size distribution, particle size, polydispersity index (PDI) and zeta potential of CST@NPs were measured by dynamic light scattering (DLS) (Malvern Instruments, UK). Transmission electron microscopic (TEM) (Hitachi, Japan) was used to characterize the morphology of CST@NPs. In addition, the high-performance liquid chromatography (HPLC) was used to evaluate the drug loading of CST in CST@NPs.

To further verify whether CST was successfully encapsulated into CST@NPs, the spectra of NPs and CST@NPs were examined by X-ray diffraction (XRD) and Fourier transform infrared spectroscopy (FTIR).

2.1.7. Acid-responsiveness evaluation of CST@NPs

CST@NPs was incubated in PBS at pH 7.4, 6.5, and 5.0, and their acid responsiveness was evaluated by Dundahl effects. At the same time, the zeta potential and morphological changes of the above nanoparticles were detected by DLS and TEM to further evaluated the acid responsiveness of CST@NPs.

To further illustrate the pH sensitivity of CST@NPs, the release properties of CST were investigated by dynamic membrane dialysis. The method was described as follows: 1 mL CST@NPs was placed in dialysis bags (3500 kDa) and incubated in 10 mL pH 7.4, 6.5 and 5.0 PBS, respectively, and incubated at 37 °C. At predetermined time points (0.5, 1, 2, 4, 8, 12 and 24 h), 1 mL of release solution was removed and supplemented with 1 mL of fresh release medium. The released CST was determined via HPLC.

2.1.8. Biodistribution of CST@NPs

To illustrate the final biodistribution of CST@NPs, the Cy5.5 was used to prepare NPs (Cy5.5@NPs) and the biodistribution was evaluated by real-time near-infrared fluorophore (NIRF). The method was described as follows: mice were administered locally with Cy5.5 and Cy5.5@NPs (Cy5.5: 0.12 mg/kg), respectively. At the presupposed time point, the mice were transferred into the machine's image chamber and anesthetized temporarily with isoflurane to visualize real-time images using an *in vivo* imaging system (IVIS). After administration for 96 h, the heart, liver, spleen, lung and kidney were dissected for *ex vivo* imaging.

2.2. Methods

2.2.1. Cell culture

HUVECs were purchased from the Cell Bank of the Chinese Academy of Science, Shanghai, China. Briefly, HUVECs were incubated in ECM medium containing 5 % fetal bovine serum (FBS) and streptomycin under standard incubation conditions (37 °C, 5 % CO_2, 95 % air). The cell culture medium was replaced every 2 days, and the cells were passaged when they reached 80–90 % density. HUVECs were categorized into five groups: Blank, H_2O_2, H_2O_2+CST, H_2O_2+NPs, and H_2O_2+CST@NPs.

2.2.2. Cell viability assay

CCK-8 was used to measure cell viability in different concentrations of hydrogen peroxide and the optimal treatment concentration and duration of treatment for CST@NPs. HUVECs in the exponential growth phase were seeded in 96-well plates at a density of 2×10^3 cells/well. Cells at 50–60 % confluence were treated with different concentrations of H_2O_2 for 24 h. Then 10 μL of CCK-8 solution was added to each well and incubated at 37 °C for 2 h. Absorbance value at 450 nm was measured using a microplate reader (SPARK 10M, Tecan, Switzerland). HUVECs stimulated by H_2O_2 were treated with different CST@NPs concentrations and times, and then absorbance values were measured in the same way.

2.2.3. *Cell live/dead assay*

To evaluate the biocompatibility of CST@NPs. HUVECs were incubated in 24-well plates (1×10^{-4} cells/mL) for 24 h, and co-incubated with PBS, H_2O_2, CST, NPs, and CST@NPs for 24 h respectively. Then, 250 μL of Calcein AM/PI assay working solution (C2015S; Beyotime Biotechnology) was added to each well of a 24-well plate and incubated at 37 °C, protected from light, for 30 min. The staining effect was observed under a fluorescence microscope (Olympus IX51, Japan). Calcein was green fluorescent and marked living cells. PI was the red fluorescent and marked dead cells. The image was analyzed as the ratio of the number of dead cells to the number of live cells in three random fields.

2.2.4. *ROS and mitochondrial potential*

The ROS (S0033S; Beyotime Biotechnology, China) assay kit was used to detect intracellular ROS. HUVECs were treated according to the established protocol. After three washes with PBS, ROS staining solution was applied and incubated at 37 °C for 30 min in dark, followed by washing with serum-free culture medium three times to diminish interference from the excess DCFDA. The fluorescence intensity of DCFDA in each group was observed under a fluorescence microscope (Olympus IX51, Japan).

2.2.5. *In vitro tubule formation assay*

Matrigel was thawed at 4 °C overnight, and then each well of the pre-cooling 96-well plate was coated with 50 μL matrigel and incubated at 37 °C for 30 min. HUVECs, which had been co-cultured with H_2O_2 (1 mM) and treatment groups (CST, NPs, CST@NPs) for 24 h, were seeded in each well (2×10^4 cells). After 3 h of incubation, incubate with Calcein AM for 30 min at 37° protected from light. Tubular structures were photographed with a microscope (Olympus IX51, Japan). The junctions were quantified using the Angiogenesis Analyzer plugin on ImageJ software.

2.2.6. *Protein extraction and Western blot*

Protein was collected from each group. RIPA lysis buffer including protease inhibitors (Sigma-Aldrich, USA) was used to lyse the HUVECs. Then, the solution was centrifuged at 12,000 rpm at 4 °C for 15 min. SDS-PAGE was used to separate proteins at 220 V. Then proteins were transferred onto 0.22 μm polyvinylidene fluoride membranes (Millipore, USA) at 400 mA. QuickBlock™ blocking buffer (PS108, Epizyme, China) was used to block the membranes at room temperature for 20 min. After incubating with specific primary antibodies (listed in Table S1) at 4 °C overnight, the samples were washed with TBST three times. Subsequently, the samples were incubated with an alkaline phosphatase–coupled secondary antibody (horseradish peroxidase-conjugated anti-rabbit immunoglobulin at 1:5000 dilution), and the bound antibody was visualized using an enhanced chemiluminescence system (Thermo Scientific, Shanghai, China). Protein expression was normalized to β-actin using ImageJ software (National Institutes of Health, NIH).

2.2.7. *Quantitative real-time PCR (qRT-PCR) analysis*

Total mRNA was isolated from HUVECs using an RNAfast 200 (Fastagen, Shanghai, China). Purified RNA was reverse transcribed into cDNA using qPCR-RT Master Mix (Toyobo, Japan). SYBR Green I dye (Toyobo, Japan) was used for monitoring DNA synthesis in the reactions. β-actin was used as an internal control to normalize the expression of numerous genes. Primers used for qRT-PCR amplification were designed, and their sequences are listed in Supplementary Table 2.

2.2.8. *Flow cytometry*

The apoptosis of HUVECs from each experimental group were detected by flow cytometry. Cells were collected into flow cytometry tubes, stained with propidium iodide (PI) and Annexin V-FITC for 15 min at room temperature away from light with a FITC Annexin V Apoptosis Detection Kit according to the manufacturer's instructions (CX006, Epizyme, China). Cell apoptosis was assayed using a CytoFLEX S flow cytometer (Beckman Coulter, USA), and the data were analyzed with FlowJo software.

2.2.9. *Immunofluorescent staining*

HUVECs cells treated as above were seeded on round coverslips within 24-well culture plates at a density of 5000 cells/well. After culturing with the different treatments for 24 h, HUVECs cells were fixed with 4 % paraformaldehyde at room temperature for 15 min. After incubated with 0.1 % Triton X-100 for 10 min, cells were blocked by 10 % goat serum for 1 h at room temperature. The coverslip was stained with the primary antibody and fluorescently labeled secondary antibody (listed in Table S3), and the nuclei were stained with DAPI (C1002; Beyotime Biotechnology). The coverslips and sections were then observed by a fluorescence microscope (Olympus IX51, Japan), and the immunofluorescence signal intensities were quantified with ImageJ software.

2.2.10. *Animals*

All the animal experiments utilized in this study were cared for in accordance with the Institutional Animal Care and Use Committee of Shandong University (Shandong, China). Genetically identified cortistatin-knockout ($CST^{-/-}$) mice with a C57BL/6N background were established by the National Resource Center of Model Mice (Nanjing, China). The murine Cort gene encodes the CST protein. To create CST-knockout mice by CRISPR/Cas9-mediated genome engineering, gRNA directed Cas9 endonuclease cleavage of the Cort gene to create double-strand breaks. These breaks were repaired by non-homologous end jointing (NHEJ), resulting in the deletion of CST [14]. Wild-type (WT) mice were purchased from the Experimental Animal Center of Shandong University. WT and $CST^{-/-}$ mice at 2 months of age were used for the experiments. Three-month-old Sprague-Dawley (SD) rats were purchased from the Animal Center of Shandong University. All of the animals were housed under controlled identical specific pathogen-free (SPF) standard environmental conditions (23 ± 2 °C, 12 h light/dark cycle) with free access to food and allowed to move freely.

2.2.11. *Human tissue*

Human skin were obtained from amputations at Qilu Hospital Shandong University, with at least five samples in each group. Briefly, the skin that was cut during the surgery was first cleaned with physiological saline and stored on ice. Subsequently, we selected the site of wound to extract skin tissue and perform pathological, western blotting assay and qRT-PCR. Patients involved in the study provided consent, and the study was approved by the medical ethics regulations of the Medical Ethical Committee of Qilu Hospital of Shandong University (KYLL-202011-103). Skin from patients with non-skin diseases was used as a control group and specimens from patients diagnosed with diabetic foot were used as an observation group.

2.2.12. *In vivo diabetic wound model*

Streptozotocin-Induced Diabetic Rat Models: Male rats (2 months old, weight: ≈180–200 g) were rendered diabetic by administering streptozotocin (60 mg/kg) intraperitoneally for 2 days after an overnight fast, as previously described [33]. Blood glucose levels were measured on Days 0, 2, 4, 6, 8, and 10 using a glucometer. Rats showing symptoms such as weight loss, polyuria, polydipsia, and a blood glucose level >16.7 mmol/L were considered diabetic. Wound healing assays were conducted on 15 diabetic rats under isoflurane inhalation anesthesia. The back of each animal was shaved, and a circular, 1.5-cm diameter, full-skin wound was created. A rubber ring was sutured around each wound to prevent skin contraction in rats. Normal rats were used as the Blank group. Diabetic rats were divided into four treatment groups: PBS group, CST group, NPs group, and CST@NPs group (delivered locally every 2 days, 15 μg/mL, 40 μL per time). Wound photographs were captured, and regular measurements and recordings of the wound area were conducted.

A diabetic mouse model (DM model) was established by intraperitoneal injection of STZ (100 mg/kg) to C57BL/6N mice for three consecutive days [34]. After the model was completed, an 8-mm wound was incised in the dorsal skin of diabetic mice and the wound was treated in the same grouping as in the diabetic rat model. A rubber ring was sutured around each wound to prevent skin contraction in mice. The untreated wound served as a control group (delivered locally every 2 days, 15 μg/mL, 20 μL per time). Wound photographs were captured, and regular measurements and recordings of the wound area were conducted.

2.2.13. *RNA sequence analysis for diabetic CST$^{-/-}$ mice*

CST$^{-/-}$ knockout mice and wild-type mice were induced as a diabetic skin total excision model, and the mice were executed after day 12 and the skin tissues were collected and stored in −80 °C. RNAseq analysis was performed by technical staff at Hangzhou Kaitai Biolab. Sequencing was carried out on a MiSeq instrument (Novaseq 6000® Sytem, Illumina Inc.). Quality examination was analyzed by an Agilent Bioanalyzer (Qseq100 DNA Analyzer, Bioptic Inc.) and real-time PCR (LightCycler® 96, Roche Inc.). Fastp was used to process raw data (https://github.com/OpenGene/fastp). Gene expression was calculated by Stringtie (https://ccb.jhu.edu/software/stringtie), and genes with FDR<0.05 and |log2FC|≥1 were considered differentially expressed genes (DEGs). Additionally, KEGG pathway enrichment analysis was performed using the R language to detect paths associated with DEGs.

2.2.14. *Histology and immunohistochemistry*

Wound skin from each group was collected and fixed in 4 % paraformaldehyde for 3 days. The samples were then dehydrated and embedded in paraffin. Each slice was then cut into 5 μm thick sections and pretreated with antigen retrieval buffer (enzymatic digestion) for 30 min at 37 °C. After blocking in goat serum for 30 min at room temperature, the sections were incubated with primary antibodies (listed in Table S4) at 4 °C overnight, followed by incubation with a horseradish peroxidase-conjugated secondary antibody for 60 min at room temperature. Detection was performed using the VECTASTAIN Elite ABC kit (Vector, Burlingame, CA, USA), and visualization was achieved by incubating with 0.5 mg/mL 3,3′-diaminobenzidine in 50 mM Tris-Cl (Sigma Aldrich). Then the slices were washed in tap water, counterstained with hematoxylin, dehydrated, and coversliped with neutral resin. Images were taken by a panoramic digital slice scanning microscope (Olympus VS120, Japan). Immunopositivity within the fields was calculated using Image-Pro Plus software.

2.2.15. *Statistical analysis*

The blinded method was used for data acquisition. Data were presented as means ± SD of results derived from three independent experiments performed in triplicate. Statistical analyses were performed with GraphPad Prism version 9.0 (GraphPad Inc., La Jolla, CA, USA) using Student's t-test (two groups) or ANOVA with Tukey's post hoc test (over two groups). The P values of 0.05 or less are considered significant.

3. Results and discussion

3.1. *Mechanism of CST in vivo*

A diabetic mouse full-thickness excision mode was fabricated using CST knockout mice and wild-type mice, and two different above skin tissues were analyzed using RNA sequencing to elucidate the mechanism of action of CST peptides *in vivo* and the pathways involved. As shown in Fig. 1A, 2520 and 2953 differentially expressed gene sequences were

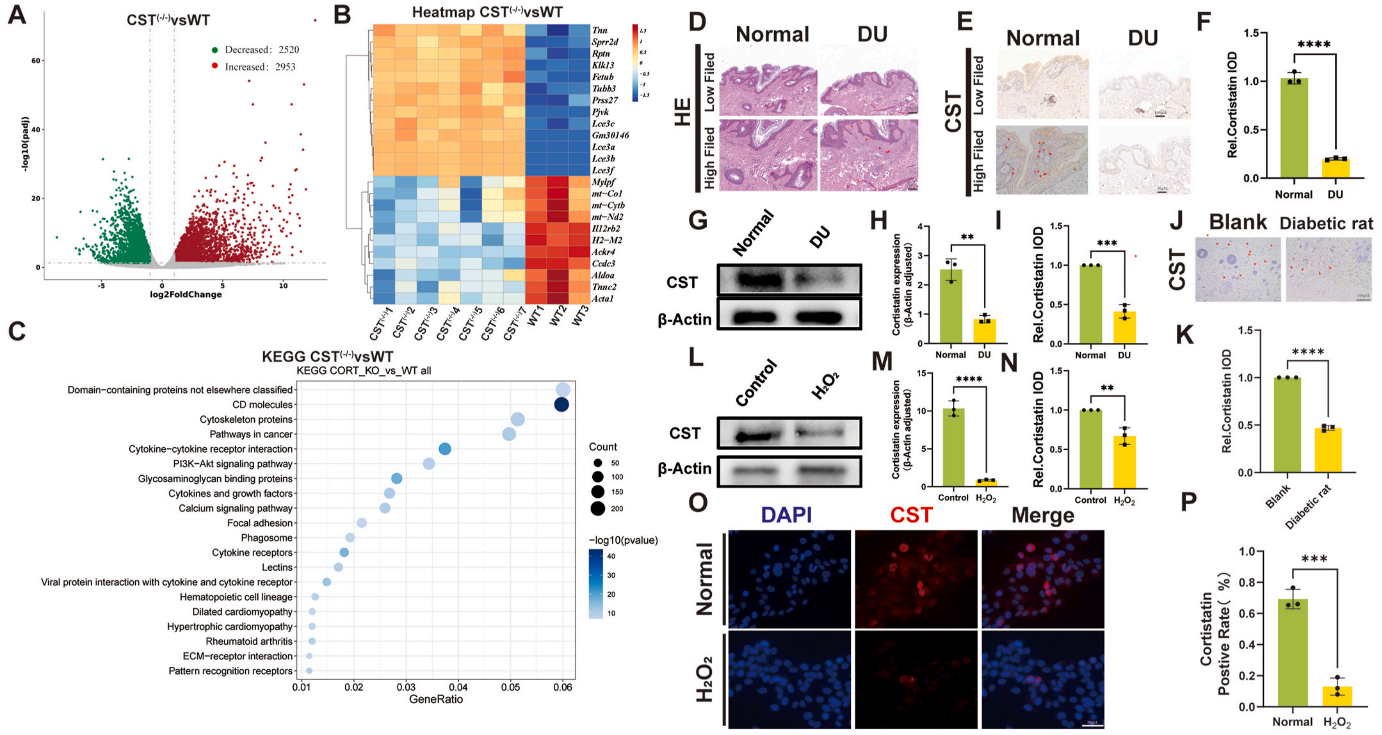

Fig. 1. RNA sequence analysis and oxidative stress reduces CST expression. (A) Volcano map of differential gene expression. (B) Microarray heatmap of the indicated groups. (C) Bubble diagram for KEGG enrichment analysis of differentially expressed genes. (Bioinformatic analysis was performed using the OmicStudio tools at https://www.omicstudio.cn/tool). (D) HE staining assay was performed on full thickness skin samples obtain from normal individuals and DU patients. (E–F) The expression level of CST in the skin of both normal individuals and diabetic ulcer patients was assessed using immunohistochemistry. (G–I) Western blotting and qRT-PCR results of CST expressing from normal individuals and diabetic ulcer patients. (J–K) CST expression assay of full thickness skin from normal individuals and DU rat models. (L–N) Western blotting and qRT-PCR results of CST expressing from normal control and H_2O_2 stimulated HUVECs. (O–P) Representative fluorescence images of CST staining of HUVECs assayed by immunofluorescence. Error bar represents mean ± SD. n = 3, ****p < 0.0001, ***p < 0.001, **p < 0.01, *p < 0.05.

upregulated and downregulated, respectively, in the CST (−/−) group compared with the control group. A heatmap was used to analyze the difference in gene expression between the control and CST (−/−) group (Fig. 1B). Compared to wild-type diabetic total skin excision mice, CST knockout diabetic total skin excision mice showed decreased expression of mt-Co1, mt-Cytb, and mt-Nd2 genes, all of which play important roles in the mitochondrial respiratory chain and are involved in the transfer of electrons in the respiratory chain as well as the synthesis of ATP, and down-regulation of these genes revealed that CST may have a potential mechanism to regulate mitochondrial function by affecting the mitochondrial respiratory chain. At the same time, the expression of Ccdc3, a gene that has been found to inhibit the activation of NFκB and thus inhibit the inflammatory response of endothelial cells, was downregulated, and the downregulation of this gene suggested an anti-inflammatory role for CST. Interestingly, the increased expression of the Lce family (Lce3a, Lce3b, Lce3c, Lce3f) is involved in the physical barrier function of the stratum corneum and is involved in innate skin defense. It has defensin-like antibacterial activity against a broad spectrum of Gram-positive and Gram-negative bacteria. This suggests that CST knockout diabetic mice may have a higher risk of infection. CST is shown in KEGG to be associated with the glycosaminoglycan-binding protein pathway (Fig. 1C), which may affect multiple biological processes and disease development. These processes include, but are not limited to, cell signaling, cell proliferation, migration, adhesion, and extracellular matrix (ECM) formation. CST may positively influence the healing process of diabetic wounds by regulating the glycosaminoglycan pathway, including promoting granulation tissue formation and angiogenesis, as well as modulating inflammatory responses.

To investigate the expression level of CST in diabetic wounds, skin samples were collected from patients with DU undergoing amputations as well as normal skin tissue from individuals with non-skin diseases. HE staining and immunohistochemistry for CST were performed. HE staining showed a higher degree of inflammatory cell infiltration in diabetic wounds, and the expression level of CST was decreased in diabetic wounds (Fig. 1D–F). Quantitative analysis of CST protein expression in the skin of patients with DU was performed using Western blot and qRT-PCR (Fig. 1G–I), revealing markedly reduced protein and mRNA expression levels of CST compared with controls. Additionally, immunohistochemistry was used to detect cutaneous tissue of diabetic and normal rats, showing a decrease in CST expression level in diabetic rats compared with normal rats (Fig. 1J–K). Further quantitative analysis using Western blot and qRT-PCR revealed decreased CST expression in cells under oxidative stress (Fig. 1L–N). Furthermore, HUVECs were cultured and grouped by whether they were stimulated by hydrogen peroxide or not, in order to observe the down-regulation of CST expression in HUVECs under oxidative stress (Fig. 1O–P). In various experiments on human skin and animal skin, it was found that diabetes causes a decrease in the expression of CST in the skin, suggesting to us that exogenous CST may be a potentially effective treatment for DUs. However, direct topical application of CST to diabetic wounds has the

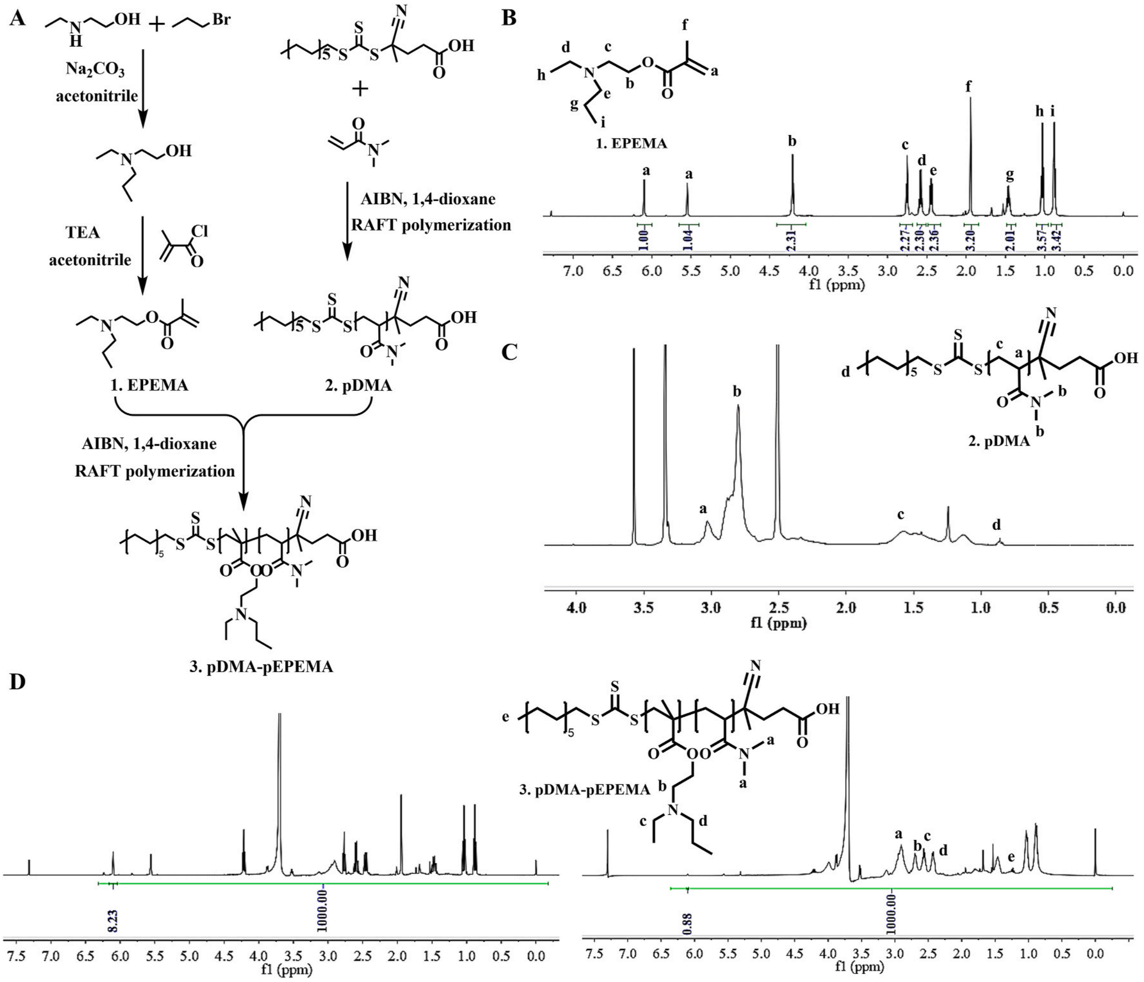

Fig. 2. The synthetic route and structural evaluation of amphiphilic polymer pDMA-pEPEMA. (A) The synthetic routes of amphiphilic polymer pDMA-pEPEMA. (B) ^{1}H NMR spectra of EPEMA proved that EPEMA have been successfully synthesized. (C) ^{1}H NMR spectra of pDMA proved that pDMA have been successfully synthesized. (D) ^{1}H NMR spectra of pDMA-pEPEMA before (T_0) and after (T_N) polymerization proved that the pDMA-pEPEMA was successfully prepared, and the monomer conversion rate of EPEMA was 89.31 %.

disadvantages of poor bioavailability and rapid degradation, so it is crucial to design a drug delivery system.

3.2. Successful synthesis of monomers EPEMA

To prepare amphiphilic polymers with pH responsiveness, protonated EPEMA was selected as the hydrophobic part of the polymer. The preparation route and structure of EPEMA are shown in Fig. 2A, and EPEMA was synthesized in two steps. The presence of tertiary ammonia in the structure allows EPEMA to be protonated in an acidic environment. The results of ^{1}H NMR confirmed the successful synthesis of EPEMA (Fig. 2B).

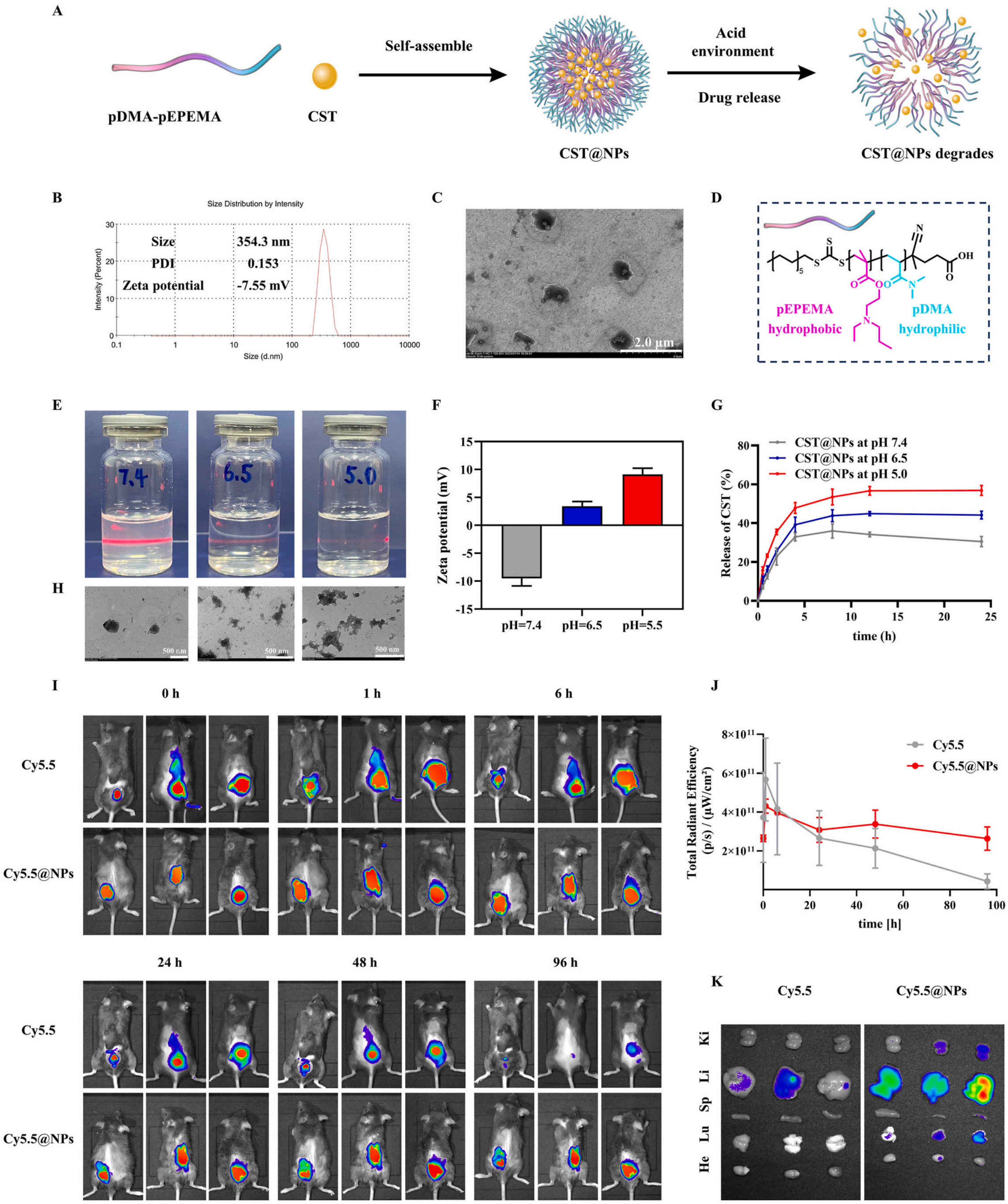

Fig. 3. Characterization, pH responsive evaluation and biodistribution of CST@NPs. (A) Schematic diagram of the preparation of CST@NPs and acid-responsive release of CST. (B) The particle size distribution, particle size (354.3 nm), PDI (0.153) and zeta potential (−7.55 mV) of CST@NPs were evaluated by DLS. (C) Representative TEM image of CST@NPs, which was demonstrated that the nanoparticles were spherical. Scale bar = 2.0 μm. (D) Schematic diagram of the structure of amphiphilic polymer pDMA-pEPEMA. Pink represents pEPEMA, the hydrophobic segment. Blue represents pDMA, the hydrophilic segment. (E) Images and Dundahl effects of CST@NPs after incubation in PBS at different pH. (F) Zeta potential of CST@NPs after incubation in PBS at different pH. (G) *In vitro* release of CST from CST@NPs after incubation in PBS at different pH levels. (H) Representative TEM images of CST@NPs after incubation in PBS at different pH. (I–K). *In vivo* imaging of diabetic C57BL/6N mice at different time points after administration with free Cy5.5 and Cy5.5@NPs, the curve of the total radiation efficiency and isolated organs after mice were sacrificed after administration for 96 h. Error bar represents mean ± SD (n = 3).

3.3. Successful polymerization of pDMA and pDMA-pEPEMA

To obtain the amphiphilic and acid-responsive homopolymer pDMA-pEPEMA, RAFT polymerization was used. Firstly, the hydrophilic polymer pDMA was prepared by RAFT polymerization, and the results of ^{1}H NMR proved that the polymerization was successful (Fig. 2C). Subsequently, the amphiphilic and acid-responsive polymer pDMA-pEPEMA was also prepared by RAFT polymerization. The results of ^{1}H NMR spectra of pDMA-pEPEMA before (T_0) and after (T_N) polymerization were showed that the pDMA-pEPEMA was successfully prepared, and the monomer conversion rate of EPEMA was 89.31 % (Fig. 2D).

3.4. Characterization of CST@NPs

As shown in Fig. 3A, the CST@NPs was prepared by nano-precipitation method. The particle size distribution, particle size, PDI, zeta potential and morphology of CST@NPs were evaluated via DLS and TEM. As shown in Fig. 3B, CST@NPs had the particle size of 354.3 nm and a uniform distribution with the PDI of 0.153. In addition, CST@NP had a zeta potential of −7.55 mV, showing the electronegativity. As shown in Fig. 3C, the image showed that CST@NP was spherical. In addition, the amount of CST loaded into CST@NPs was evaluated by HPLC. The results showed that the drug loading was 15.51 ± 0.58 % and the encapsulation efficiency was 73.47 ± 3.29 %.

Since the standard PDF card for CST was not retrieved, the peak location was contrasted by using the CST standard as a control. As shown in Fig. S1, the results shown that in the XRD pattern of CST@NPs, there are two diffraction peaks of CST, which proved that CST was successfully loaded into CST@NPs. However, the peak intensity is weak, which was caused by the low content of CST and that CST was loaded into the interior of the nanoparticles. As shown in Fig. S2, in the FTIR pattern of CST@NPs, there was C=C (1689 cm^{-1}) stretching vibration absorption peak, and there was (amide II band) N-H (1538 cm^{-1}) bending vibration absorption peak, which were the characteristic group peaks of CST. Similarly, the absorption peak intensity is relatively weak because the CST was encapsulated in the interior of CST@NPs. The results were mutually verified with the data in the XRD pattern.

The above results proved that the CST@NPs was successfully prepared and the CST was successfully encapsulated into the interior of CST@NPs.

3.5. Acid-responsiveness evaluation of CST@NPs

In acidic environment, EPEMA in the amphiphilic polymer pDMA-pEPEMA was protonated, which destabilized the nanoparticle structure and caused the nanoparticle to disaggregate, triggering the responsive release of CST. Therefore, the different drug release in CST@NPs under different pH conditions is due to the different structural damage of the CST@NPs. Under different pH conditions, the degradation trend of CST@NPs should be the same as the drug release trend. Firstly, acid-responsive depolymerization of CST@NPs was preliminarily demonstrated by the attenuated Dundahl effect after incubation of the nanoparticles in pH 6.5 and 5.0 PBS (Fig. 3E). To further demonstrate the acid-responsive depolymerization of CST@NPs, the morphology and zeta potential of the nanoparticles after incubation in different pH PBS were evaluated by TEM and DLS. The results showed that with the decrease of pH (the increase of acidity), the CST@NPs gradually degraded (Fig. 3E and H) and the potential flipped to positive (Fig. 3F), demonstrating the acid responsiveness of CST@NPs.

In addition, the *in vitro* release characteristics of CST were investigated by dynamic membrane dialysis method. As shown in Fig. 3G, When CST@NPs was incubated in pH 7.4 PBS, the minimal release of CST (30.51 ± 2.12 %) was observed. In contrast, When CST@NPs was incubated in pH 6.5 and 5.0 PBS, the CST release percentage were 44.17 ± 1.63 % and 56.90 ± 2.09 %, demonstrating the pH-responsiveness release of CST. At the same time, the kinetics of CST release profile was analyzed by different release kinetic models to determine the release mechanism. As shown in Fig. S3 and Table S1, we determined that the release mechanism of CST was consistent with the first-order kinetic model.

3.6. Biodistribution of CST@NPs

The distribution of the drugs after administered locally in mice (containing diabetic wounds) was evaluated. Cy5.5@NPs was prepared by using Cy5.5 as a NIR fluorescent molecule instead of CST. As shown in Fig. 3I–K, NPs can significantly enhance the retention time of drugs and increase the efficacy. In addition, both free drug and NPs can enter the blood circulation to achieve distribution in major organs. In addition, the metabolism of NPs was slowed down *in vivo* compared with free drug.

3.7. CST@NPs rescue mitochondrial dysfunction

First, the efficiency of H_2O_2 in cell viability was assessed in HUVECs through a CCK8 assay, which revealed 1 mM as the ideal concentration of H_2O_2 in HUVECs to induce oxidative stress effectively. The optimal therapeutic concentration of CST@NPs was 15 μg/mL (Fig. S4A-C). Subsequently, the live/dead assay was performed in HUVECs, and image acquisition was performed after 24 h of incubation (Fig. 4B–E), which showed that there was no significant difference in the proportion of live-dead cells between the CST@NPs group and the Blank group. These experiments demonstrated the biocompatibility of CST@NPs, which were not toxic to cells at a concentration of 15 μg/mL.

Activation of cell proliferation is an essential step in wound healing, whereas oxidative stress disrupts the proliferative behavior of various cell types. ROS are key regulators at all stages of wound healing, with low levels potentially aiding in bacterial resistance and promoting wound healing. However, the hyperglycemic acidic microenvironment in diabetic wounds leads to excessive production of ROS, resulting in a redox imbalance that hinders wound healing. Our *in vitro* experiments using HUVECs demonstrate that CST@NPs treatment significantly attenuates ROS production, indicating a potential mechanism for the enhanced healing observed (Fig. 4C–F). Mitochondria play a crucial role in cell apoptosis, and the disruption of mitochondrial membrane potential is an early event in the apoptotic cascade. Our results show that CST@NPs treatment maintains mitochondrial membrane potential closer to normal levels compared with the H_2O_2 group (Fig. 4D,G), suggests that CST@NPs are protective against oxidative stress-induced mitochondrial apoptosis.

Oxidative stress and increased ROS levels are known to contribute to vascular endothelial dysfunction and apoptosis, exacerbating the impaired healing process. Our study employs various assays, including flow cytometry (Fig. 4I), immunofluorescence of caspase-3 (Fig. 4J), Western blot (Fig. 4K), and real-time PCR for apoptosis-related markers, such as Bax, Bcl-2, and cleaved caspase-3, all indicating that CST@NPs effectively attenuate apoptosis induced by oxidative stress (Fig. 4L–Q). In the above experiments we found that CST@NPs were able to reverse the excess accumulation of reactive oxygen species and apoptosis caused by oxidative stress, and restore the proliferative vigor of cells.

3.8. CST@NPs facilitates angiogenesis, cellular proliferation, and exerts anti-inflammatory effects

Angiogenesis and cellular proliferation are critical aspects of wound healing, particularly in diabetic wounds with poor vascularization. Robust angiogenesis ensures efficient delivery of oxygen and nutrients to the wound site, enhancing tissue repair. Using a Matrigel tube formation assay, the tube-forming capacity of HUVECs was demonstrated. As indicated in Fig. 5A and C, the number of junctions at 3 h was remarkably higher in CST@NPs groups compared with H_2O_2 alone. Additionally, In the current study, Ki67, a sensitive biomarker of cell

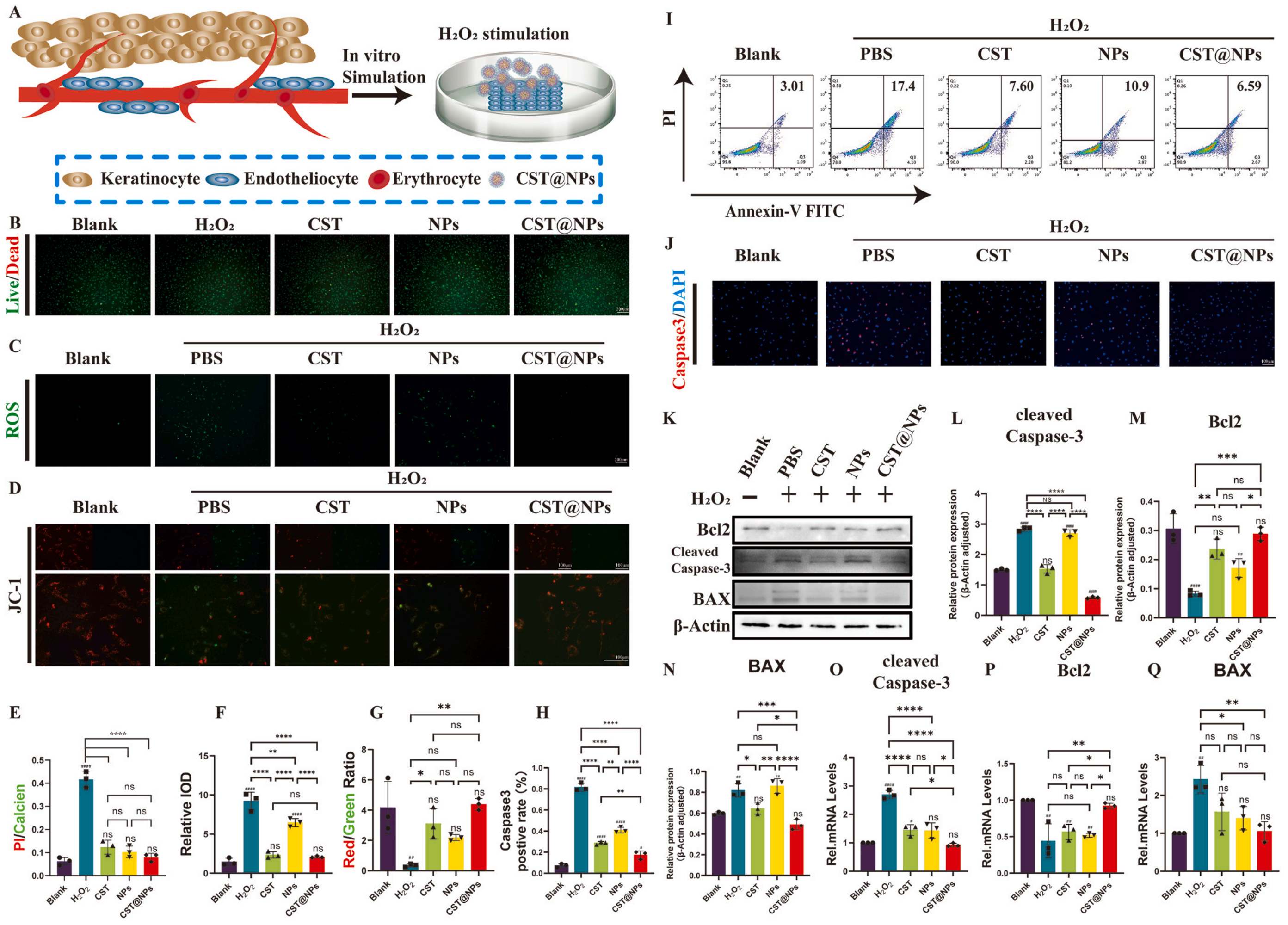

Fig. 4. CST@NPs rescue mitochondrial dysfunction (A) Schematic representation of *in vitro* experiments with HUVECs. (B) Representative images and quantitative analysis of Live/Dead staining in HUVECs. (C) Representative images of ROS staining in different experimental groups. (D) Mitochondrial membrane potential of HUVECs assessed through JC-1 assay. (E–H) Quantitative analysis of Live/Dead staining, ROS staining, JC-1 staining, Caspase-3 immunofluorescence staining. (I) The apoptosis rate of each experimental group of HUVECs, as measured by flow cytometry. (J) Representative fluorescence images of caspase 3 staining (red) of HUVECs and quantitative analysis. (K–Q) The expression of apoptosis-related proteins and mRNA (Bcl-2, cleaved Caspase-3, and BAX) on HUVECs with different treatments. Error bar represents the mean ± SD. n = 3, ****p < 0.0001, ***p < 0.001, **p < 0.01, *p < 0.05. p < 0.0001, p < 0.001, p < 0.01, p < 0.05 vs Blank group.

proliferation, was used to determine the effect of CST@NPs on HUVECs cell proliferation. CST@NPs maintain the proliferative capacity of cells under oxidative stress, as evidenced by the maintenance of Ki-67-positive cells, further supporting their role in enhancing wound healing (Fig. 5B and D).

The Western blot and qRT-PCR results revealed an upregulation of inflammatory cytokines (COX-2 and iNOS) after H_2O_2 stimulation in HUVECs. On the contrary, the expression of pro-angiogenic factors such as CD31 and VEGF was downregulated, signifying that H_2O_2 stimulation induced an inflammatory response and impaired angiogenesis. However, CST@NPs showed remarkable efficacy in mitigating the H_2O_2-induced inflammatory response in HUVECs while showing significant advantages over other treatment groups in promoting neovascularization (Fig. 5E–K). This result suggests that CST@NPs can alleviate the persistent inflammatory response of diabetic wounds and promote the generation of small surrounding blood vessels to provide sufficient oxygen, nutrients, and growth factors to accelerate the healing of diabetic wounds.

3.9. *In vivo wound healing capacity of CST@NPs*

Using a full-thickness excision model in diabetic rats, we assessed the *in vivo* promotion of wound closure by CST@NPs. A 1.5-cm incision was made on the dorsal skin of diabetic rats and subsequently treated according to the assigned groups. Non-diabetic wounds and untreated diabetic wounds were used as negative and positive control groups, respectively (Fig. 6A). Throughout the observation period, the wound area in all groups exhibited a gradual decrease. Skin wound healing was significantly accelerated in diabetic rats after CST, NPs and CST@NPs interventions compared to the PBS group. By the fourth day, the skin wound area in the Blank and CST@NPs groups appeared significantly different from the other three groups, and complete wound healing was observed in the Blank and CST@NPs groups on the 10th postoperative day, with a significantly better therapeutic efficacy than that of the other control groups (Fig. 6B–E).

Granulation tissue, which consists of nascent capillaries, proliferating fibroblasts, and inflammatory cells, is able to rapidly fill the wound defect and can be used as an important indicator of wound healing. Statistical analysis (Fig. 6G–H) of HE (Fig. 6C) and Masson Trichrome (Fig. 6D) staining showed that CST@NPs induced the formation of granulation tissue in wounds, enhanced collagen deposition. In the immunohistochemical analysis of the wounds, the CST@NPs-treated group showed a decrease in the expression of COX-2 (Fig. S5A) and iNOS (Fig. S5B) compared with the control group, which indicated that

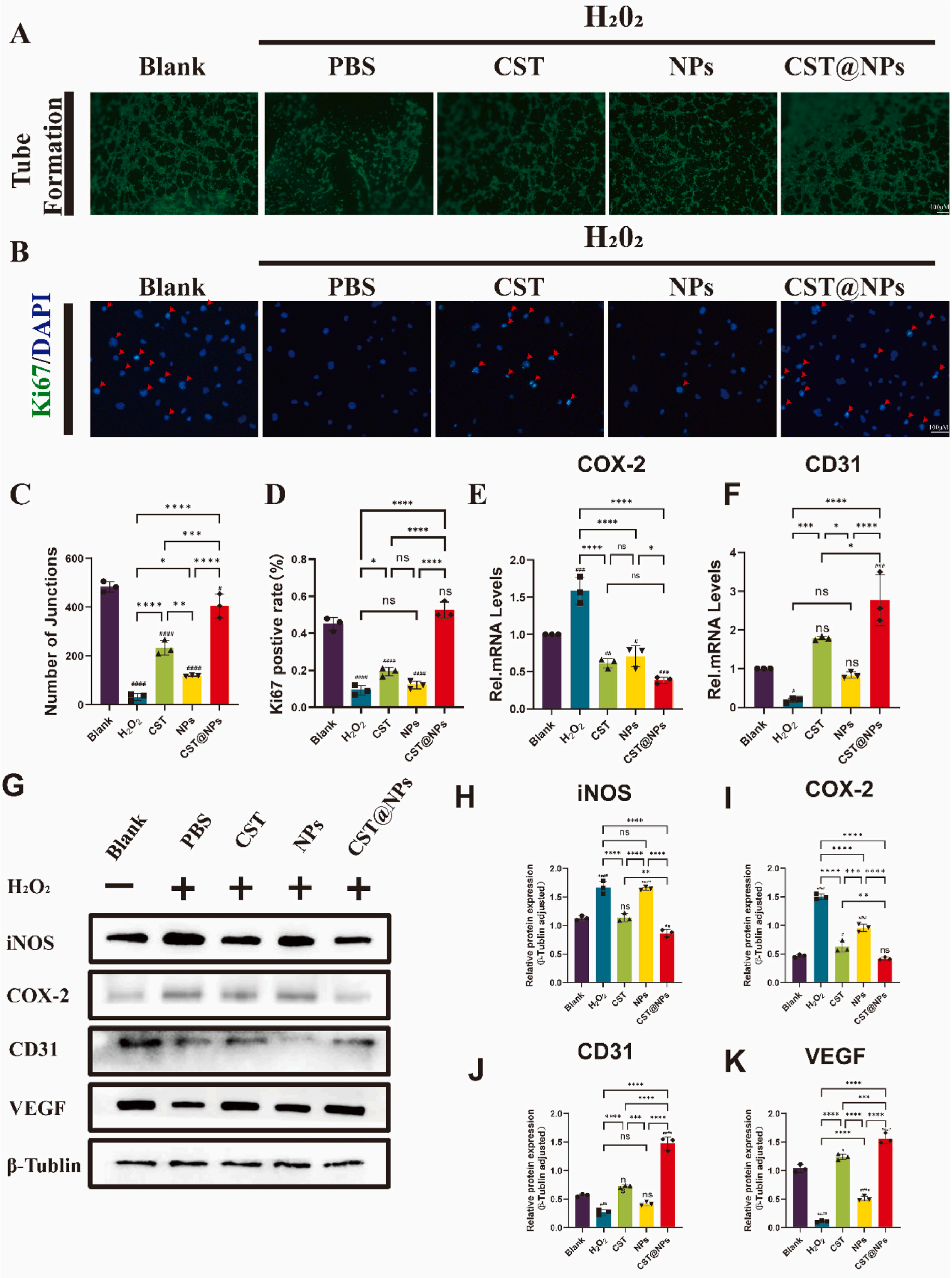

Fig. 5. Vasculogenic capacity and anti-inflammatory effect of CST@NPs *in vitro*. (A) Representative images of the tube formation assay in HUVECs. (B) Representative fluorescence images of Ki67 staining (green) of HUVEC cells. Red arrows indicate Ki67-positive cells. (C) Quantitative measurement of the number of junctions. (D) Quantitative measurement of Ki67-positive cell population. (E–K) The expression of inflammatory cytokines (iNOS and COX-2) and vascularization-related proteins (CD31 and VEGF) and mRNA on HUVECs with different treatments. Error bar represents the mean ± SD. n = 3, ****$p < 0.0001$, ***$p < 0.001$, **$p < 0.01$, *$p < 0.05$. ####$p < 0.0001$, ###$p < 0.001$, ##$p < 0.01$, #$p < 0.05$ vs Blank group.

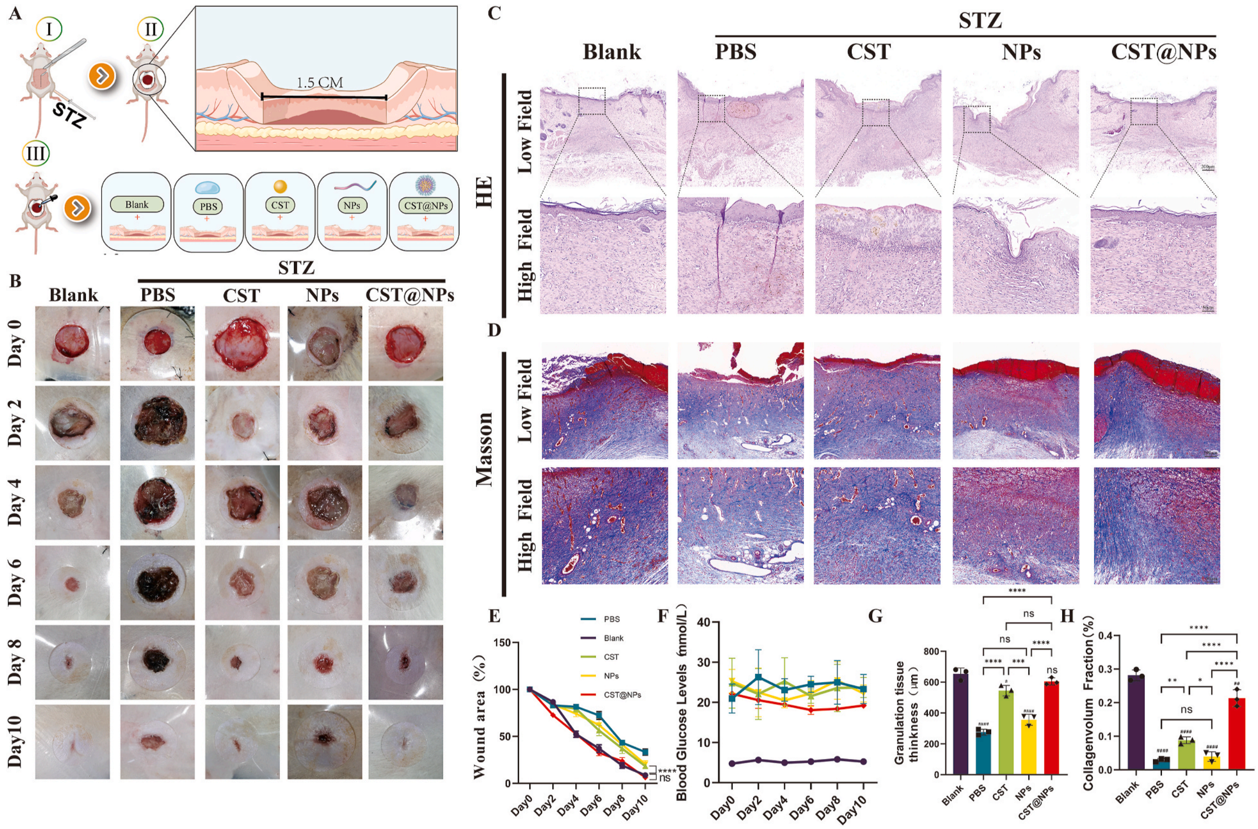

Fig. 6. CST@NPs promotes wound healing in diabetic rats. (A) An illustration of the full-thickness excision model in diabetic rats. (B) The representative photographs of wounds in diabetic rats were captured from day 0 to day 10. (C) H&E staining and granulation tissue thickness of each group on the 10th day. (D) Masson Trichrome staining and deposition of collagen of each group on the 10th day. (E) Percentage of wound at 2, 4, 6, 8, and 10 days in different experimental groups. (F) The blood glucose levels of the five groups. (G–H) Statistical chart of H&E and Masson Trichrome staining. Error bar represents the mean ± SD. n = 3, ****$p < 0.0001$, ***$p < 0.001$, **$p < 0.01$, *$p < 0.05$. ####$p < 0.0001$, ###$p < 0.001$, ##$p < 0.01$, #$p < 0.05$ vs Blank group.

CST@NPs had an anti-inflammatory effect and was able to attenuate the inflammatory response of diabetic wounds (Figs. S5E–G). In addition, the expression levels of VEGF (Fig. S5D) and CD31 (Fig. S5C) were significantly increased in the CST@NPs-treated group. VEGF is a key angiogenic factor that promotes neovascularization, whereas the increased expression of CD31, an endothelial cell marker, reflects neovascularization. These results suggest that CST@NPs promoted neovascularization of diabetic wounds by up-regulating the expression of VEGF and CD31 (Figs. S5H–I), inducing the formation of more small blood vessels in the granulation tissues, which in turn feeds back to the thickening of the granulation tissues and provides oxygen as well as nutrients for the healing of the tissues. These findings suggest that CST@NPs effectively enhance wound healing in diabetic rats by attenuating inflammation, promoting angiogenesis, promoting maturation and thickening of granulation tissue and facilitating collagen deposition, thereby expediting the transition from the inflammatory stage to the healing and remodeling stage.

In a total skin excision model of diabetic mice, we performed a 12-day wound healing observation. The CST@NPs-treated group showed significant wound healing at day 12 (Fig. 7A), and more complete wound healing was observed in the CST@NPs group compared to the CST control group. In addition, diabetic CST knockout mice showed poorer wound healing compared to diabetic wild-type mice, suggesting that CST deficiency may exacerbate the difficulty of healing diabetic wounds. By performing HE staining (Fig. 7D) and Masson staining (Fig. 7E) of the wounds, we observed that the granulation tissue thickness in the CST@NPs group was similar to that of the negative control mice, and collagen deposition was superior to that of the CST group (Fig. 7F–G), whereas the diabetic CST knockout mice were inferior to the diabetic normal mice in terms of both the granulation tissue thickness and the collagen scores. This finding points to the fact that the presence of CST is critical for granulation tissue formation and wound healing. We also performed immunohistochemical staining for CD31 to assess neovascularization (Figs. S6A–B). In the CST@NPs-treated group, the expression level of CD31 was similar to that of the negative control group, suggesting that CST@NPs can promote angiogenesis in the granulation tissue, which helps to provide more oxygen and nutrients to the trauma and accelerate the wound healing process. In contrast, diabetic CST knockout mice had reduced levels of CD31 expression, which is consistent with their poorer healing.

Thus, CST@NPs significantly improved wound healing in diabetic mice by promoting granulation tissue formation and angiogenesis. These findings provide an experimental basis for CST@NPs as a potential therapy for diabetic wound treatment.

4. Discussion

DUs are a serious complication that endangers people with diabetes and can cause systemic damage and even death. The management of diabetic wounds is a major challenge because these wounds in diabetic patients often exhibit slow or impaired healing, with delayed healing increasing the risk of infection. In fact, individuals with diabetes who develop foot ulcers face a mortality risk that is 2.5 times higher within a 5-year timeframe [35]. In previous studies we have found CST is a cyclic neuropeptide that displays multiple properties in several physiological as well as disease processes. Recent findings in types of models have indicated that CST might represent a natural, endogenous protective factor against disorganization of apoptosis as well as metabolism,

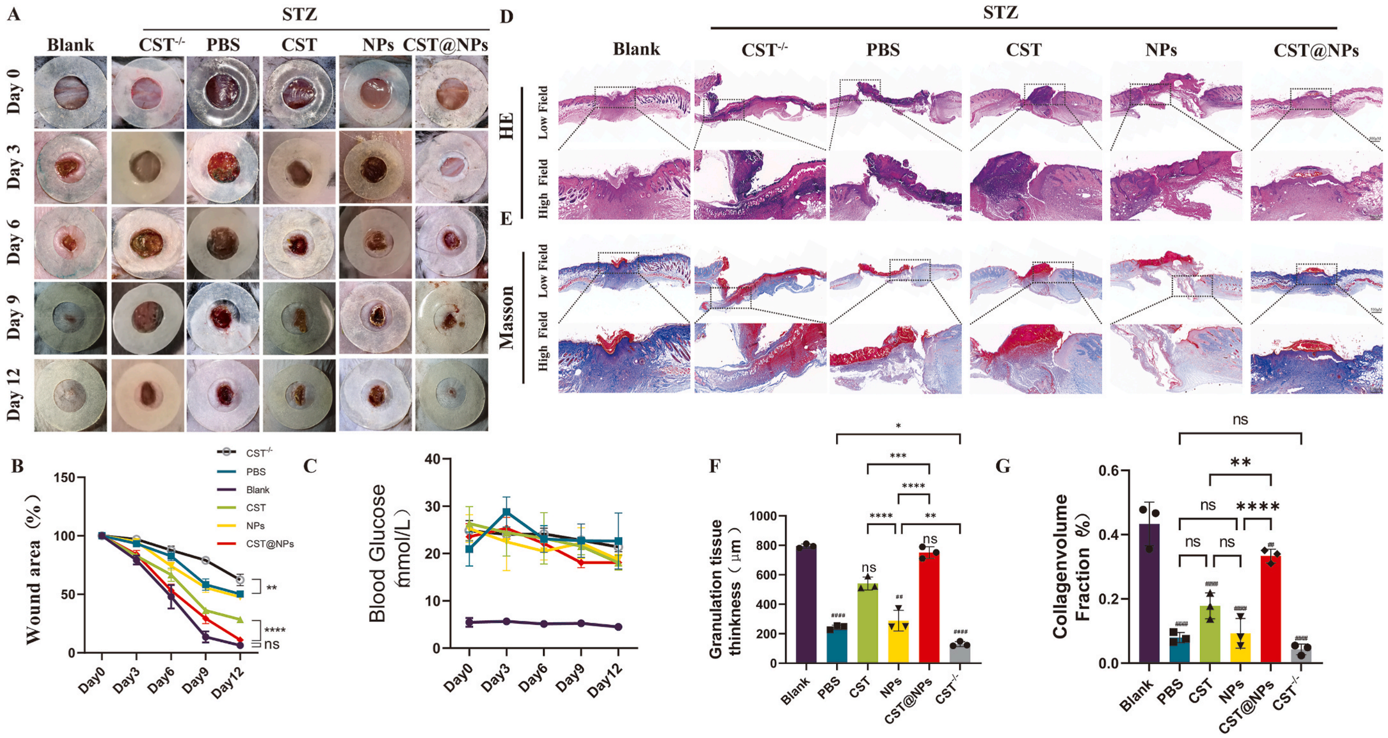

Fig. 7. CST@NPs promotes skin healing in diabetic mice. (A) The representative photographs of wounds in diabetic mice were captured from day 0 to day 12. (B) Percentage of wound at 2, 4, 6, 8, 10 and 12 days in different experimental groups. (D–G) H&E staining and Masson Trichrome staining of each group on the 12th day and quantitative statistical charts. Error bar represents the mean ± SD. n = 3, $****p < 0.0001$, $***p < 0.001$, $**p < 0.01$, $*p < 0.05$. $\#\#\#\#p < 0.0001$, $\#\#\#p < 0.001$, $\#\#p < 0.01$, $\#p < 0.05$ vs Blank group.

exhibits powerful anti-inflammatory effects. However, CST may have the disadvantages of low bioavailability and short duration of drug action when acting directly on diabetic wounds. Therefore, in-depth study of the molecular mechanism of CST to promote the healing of diabetic wounds and the design of drug delivery systems that can enhance the effects of CST are essential to promote diabetic wounds.

Under oxidative stress, the overproduction of ROS exacerbates the inflammatory response at the skin defect, leading to a decrease in local pH. Inflammation of the skin defect results in a lower local pH than that of normal tissue. Bacterial metabolism of diabetic wounds produces lactic acid and acetic acid, which further contribute to the reduction of local pH and inflammation [36–39]. In the current study, we proposed a potential strategy for enhancing wound healing treatment efficiency in DUs. As the core of our strategy for wound healing treatment, We have developed CST@NPs and made them acid-responsive by combining CST with the amphiphilic polymer pDMA-pEPEMA [40–42]. As a result, acid-responsive release CST nanoparticles can act more precisely in localized low pH environments to continuously release CST and promote wound healing.

We found that CST expression was decreased in diabetic patients in skin sections, which suggested that CST may play a potential role in the healing of diabetic wounds. In order to determine the mechanism of action of CST, RNA sequencing of the skin wound of $CST^{-/-}$ diabetic mice versus wild-type diabetic mice was used in the study. Interestingly, it turned out that the mitochondrial of $CST^{-/-}$ mice related genes (mt-Co1, mt-Cytb, and mt-Nd2) as well as anti-inflammatory genes (Ccdc3) were decreased in expression, leading to the inhibition of the respiratory chain, causing impaired energy metabolism, and ultimately leading to apoptosis or cell death. Meanwhile, the expression of some genes with defensin-like antimicrobial activity (Lce3a, Lce3b, Lce3c, Lce3f) was up-regulated, This may be associated with an elevated risk of infection due to reduced granulation tissue thickness in the healing skin of CST knockout mice. In summary, CST may promote diabetic wound healing by anti-inflammatory and rescuing mitochondrial apoptosis.

It is known that mitochondrial function plays a critical role in viability of proliferation of small blood vessel cells. In follow-up *in vitro* study, H_2O_2 administration imitated the oxidative stress environment of HUVECs in diabetic wounds and led to mitochondrial dysfunction and enhanced apoptosis of HUVECs, which is in consistence with previous reports [43,44]. Due to the antioxidant and anti-inflammatory properties of CST, the CST@NPs group decreased the expression of intracellular ROS, reduced cellular mitochondrial damage, inhibited apoptosis, and maintained the expression of intracellular Ki-67, which reversed the cellular proliferative capacity as well as the ability of small vessel formation [14,36,45,46]. And in line with our expectations, the CST@NPs showed better treatment outcomes compared to the free CST. In our study, to represent the diversity of human diabetic patients, we chose streptozotocin (STZ)-induced rat as well as mouse diabetic models to study impaired wound healing mechanisms [34]. In addition, the *in vivo* experiments were consistent with previous experiments, and in both rat and mouse diabetic skin total excision models, the skin healing rate of the CST@NPs group was significantly better than that of the PBS group, and there was no statistically significant difference from that of the nondiabetic model group. Histological experiments have revealed that CST promotes skin healing by accelerating reepithelialization, improving granulation tissue formation [2], promoting collagen deposition at the wound site, down-regulating inflammatory mediator expression and increasing neovascularization to promote diabetic wound healing.

This study provides a promising treatment modality for clinically distressed patients with DUs and offers valuable insights into the management of patients with diabetic ulcers [36,47–51].

5. Conclusion

In summary, an CST-loaded pDMA-pEPEMA nanoparticles (CST@NPs) was developed to efficiently deliver CST into the low-PH microenvironment for treatment of DUs. The results showed that

CST@NPs promoted wound healing in a diabetic wound model by rescuing oxidative stress-induced mitochondrial dysfunction, promoting re-epithelialization, granulation tissue formation, collagen deposition, angiogenesis and wound contraction. This study not only reveals a new mechanism of diabetic wound healing, but also provides a potential new therapy for diabetic patients, which is expected to improve the prognosis and quality of life of diabetic patients.

Ethics approval and consent to participate

All animal experiments in this study were performed in accordance with institutional guidelines and approved by the Laboratory Animal Center of Qilu Hospital of Shandong University (KYLL-2020(KS)-308). The study of human tissue was approved by the institutional review board of Qilu Hospital of Shandong University (KYLL-202011-103).

Data availability statement

The data that support the findings of this study are available from the corresponding author upon reasonable request.

Declaration of competing interest

The authors declare no conflict of interest.

CRediT authorship contribution statement

Xuelian Zhang: Methodology, Investigation, Formal analysis, Data curation, Conceptualization. **Hang Li:** Investigation, Formal analysis, Data curation, Conceptualization. **Yang Liu:** Methodology, Investigation, Formal analysis, Data curation, Conceptualization. **Jie Yu:** Investigation, Formal analysis, Data curation, Conceptualization. **Pengfei Zhang:** Software, Resources, Project administration, Methodology. **Peiling Yu:** Software, Resources, Project administration, Methodology. **Yuhao Liu:** Software, Resources, Project administration, Methodology. **Suyi Jia:** Software, Resources, Project administration, Methodology. **Lijuan Ling:** Investigation. **Peng Li:** Software, Resources, Project administration, Methodology. **Lei Li:** Software, Resources, Project administration, Methodology. **Yueyao Wang:** Software, Resources, Project administration, Methodology. **Tengxiao Huang:** Software, Resources, Project administration, Methodology. **Gaoxin Jin:** Software, Resources, Project administration, Methodology. **Yunpeng Zhao:** Software, Resources, Project administration, Methodology. **Guoli Ma:** Software, Resources, Project administration, Methodology. **Qinghao Yuan:** Software, Resources, Project administration, Methodology. **Lei Zhu:** Writing – review & editing, Writing – original draft, Visualization, Validation, Supervision. **Zhiyue Zhang:** Writing – review & editing, Writing – original draft, Visualization, Validation, Supervision. **Hao Li:** Writing – review & editing, Writing – original draft, Visualization, Validation, Supervision. **Weiwei Li:** Writing – review & editing, Writing – original draft, Visualization, Validation.

Acknowledgements

This work was supported by the National Natural Science Foundation of China (Grant No. 82072478to Yunpeng Zhao; Grant No. 82073437to Weiwei Li), Shandong Provincial Natural Science Foundation (Grant No. ZR2020YQ54, to Yunpeng Zhao). We would like to acknowledge the technical support from the Shandong University Research Center for Basic Medical Sciences. Meanwhile, we thank the Translational Medicine Core Facility of Shandong University for the consultation and instrument availability that supported this work.

Appendix A. Supplementary data

Supplementary data to this article can be found online at https://doi.org/10.1016/j.bioactmat.2024.10.004.

References

[1] J. Zhao, T. Xu, J. Sun, H. Yuan, M. Hou, Z. Li, J. Wang, Z. Liang, Multifunctional nanozyme-reinforced copper-coordination polymer nanoparticles for drug-resistance bacteria extinction and diabetic wound healing, Biomater. Res. 27 (1) (2023) 88.

[2] B. Kandregula, S. Narisepalli, D. Chitkara, A. Mittal, Exploration of lipid-based nanocarriers as drug delivery systems in diabetic foot ulcer, Mol. Pharm. 19 (7) (2022) 1977–1998.

[3] W. Zhang, K. Zha, Y. Xiong, W. Hu, L. Chen, Z. Lin, C. Yu, W. Zhou, F. Cao, H. Hu, B. Mi, G. Liu, Glucose-responsive, antioxidative HA-PBA-FA/EN106 hydrogel enhanced diabetic wound healing through modulation of FEM1b-FNIP1 axis and promoting angiogenesis, Bioact. Mater. 30 (2023) 29–45.

[4] Y. Xiong, X. Chu, T. Yu, S. Knoedler, A. Schroeter, L. Lu, K. Zha, Z. Lin, D. Jiang, Y. Rinkevich, A.C. Panayi, B. Mi, G. Liu, Y. Zhao, Reactive oxygen species-scavenging nanosystems in the treatment of diabetic wounds, Adv. Healthcare Mater. 12 (25) (2023) e2300779.

[5] Y. Xiong, B.B. Mi, Z. Lin, Y.Q. Hu, L. Yu, K.K. Zha, A.C. Panayi, T. Yu, L. Chen, Z. P. Liu, A. Patel, Q. Feng, S.H. Zhou, G.H. Liu, The role of the immune microenvironment in bone, cartilage, and soft tissue regeneration: from mechanism to therapeutic opportunity, Mil Med Res 9 (1) (2022) 65.

[6] Y. Xiong, Z. Lin, P. Bu, T. Yu, Y. Endo, W. Zhou, Y. Sun, F. Cao, G. Dai, Y. Hu, L. Lu, L. Chen, P. Cheng, K. Zha, M.A. Shahbazi, Q. Feng, B. Mi, G. Liu, A whole-course-repair system based on neurogenesis-angiogenesis crosstalk and macrophage reprogramming promotes diabetic wound healing, Adv. Mater. 35 (19) (2023) e2212300.

[7] Y. Jiang, X. Feng, X. Qiao, Y. Li, X. Li, J. Yang, L. Han, Plant-inspired visible-light-driven bioenergetic hydrogels for chronic wound healing, Bioact. Mater. 41 (2024) 523–536.

[8] H. Zhu, J. Zheng, X.Y. Oh, C.Y. Chan, B.Q.L. Low, J.Q. Tor, W. Jiang, E. Ye, X. J. Loh, Z. Li, Nanoarchitecture-integrated hydrogel systems toward therapeutic applications, ACS Nano 17 (9) (2023) 7953–7978.

[9] E. Gonzalez-Rey, N. Varela, A.F. Sheibanie, A. Chorny, D. Ganea, M. Delgado, Cortistatin, an antiinflammatory peptide with therapeutic action in inflammatory bowel disease, Proc. Natl. Acad. Sci. U. S. A. 103 (11) (2006) 4228–4233.

[10] M. Barriga, R. Benitez, V. Ferraz-de-Paula, M. Garcia-Frutos, M. Caro, G. Robledo, F. O'Valle, J. Campos-Salinas, M. Delgado, Protective role of cortistatin in pulmonary inflammation and fibrosis, Br. J. Pharmacol. 178 (21) (2021) 4368–4388.

[11] V. Delgado-Maroto, C.P. Falo, I. Forte-Lago, N. Adan, M. Morell, E. Maganto-Garcia, G. Robledo, F. O'Valle, A.H. Lichtman, E. Gonzalez-Rey, M. Delgado, The neuropeptide cortistatin attenuates experimental autoimmune myocarditis via inhibition of cardiomyogenic T cell-driven inflammatory responses, Br. J. Pharmacol. 174 (3) (2017) 267–280.

[12] S. Zhu, B. Zhao, M. Li, H. Wang, J. Zhu, Q. Li, H. Gao, Q. Feng, X. Cao, Microenvironment responsive nanocomposite hydrogel with NIR photothermal therapy, vascularization and anti-inflammation for diabetic infected wound healing, Bioact. Mater. 26 (2023) 306–320.

[13] Y. Zhao, C. Qiu, W. Wang, J. Peng, X. Cheng, Y. Shangguan, M. Xu, J. Li, R. Qu, X. Chen, S. Jia, D. Luo, L. Liu, P. Li, F. Guo, K. Vasilev, L. Liu, J. Hayball, S. Dong, X. Pan, Y. Li, L. Guo, L. Cheng, W. Li, Cortistatin protects against intervertebral disc degeneration through targeting mitochondrial ROS-dependent NLRP3 inflammasome activation, Theranostics 10 (15) (2020) 7015–7033.

[14] Y. Zhao, Y. Li, R. Qu, X. Chen, W. Wang, C. Qiu, B. Liu, X. Pan, L. Liu, K. Vasilev, J. Hayball, S. Dong, W. Li, Cortistatin binds to TNF-α receptors and protects against osteoarthritis, EBioMedicine 41 (2019) 556–570.

[15] R. Cheng, L. Jiang, H. Gao, Z. Liu, E. Mäkilä, S. Wang, Q. Saiding, L. Xiang, X. Tang, M. Shi, J. Liu, L. Pang, J. Salonen, J. Hirvonen, H. Zhang, W. Cui, B. Shen, H. A. Santos, A pH-responsive cluster metal-organic framework nanoparticle for enhanced tumor accumulation and antitumor effect, Adv. Mater. 34 (42) (2022) e2203915.

[16] R. Hu, X. Chen, Z. Li, G. Zhao, L. Ding, L. Chen, C. Dai, Y. Chen, B. Zhang, Liquid nanoparticles for nanocatalytic cancer therapy, Adv. Mater. 35 (48) (2023) e2306469.

[17] Y. Zhao, C. Shi, X. Yang, B. Shen, Y. Sun, Y. Chen, X. Xu, H. Sun, K. Yu, B. Yang, Q. Lin, pH- and temperature-sensitive hydrogel nanoparticles with dual photoluminescence for bioprobes, ACS Nano 10 (6) (2016) 5856–5863.

[18] Y.J. Liu, S.H. Dong, W.H. Hu, Q.L. Chen, S.F. Zhang, K. Song, Z.C. Han, M.M. Li, Z. T. Han, W.B. Liu, X.S. Zhang, A multifunctional biomimetic nanoplatform for image-guideded photothermal-ferroptotic synergistic osteosarcoma therapy, Bioact. Mater. 36 (2024) 157–167.

[19] W. Yao, Z. Song, X. Ma, Y. Huang, X. Zhang, Y. Li, P. Wei, J. Zhang, C. Xiong, S. Yang, Y. Xu, W. Jing, B. Zhao, X. Zhang, Y. Han, Asymmetric adhesive SIS-based wound dressings for therapeutically targeting wound repair, J. Nanobiotechnol. 22 (1) (2024) 34.

[20] H. Yu, Z. Song, J. Yu, B. Ren, Y. Dong, Y. You, Z. Zhang, C. Jia, Y. Zhao, X. Zhou, H. Sun, X. Zhang, Supramolecular self-assembly of EGCG-selenomethionine nanodrug for treating osteoarthritis, Bioact. Mater. 32 (2024) 164–176.

[21] A.G. Kurian, R.K. Singh, V. Sagar, J.H. Lee, H.W. Kim, Nanozyme-engineered hydrogels for anti-inflammation and skin regeneration, Nano-Micro Lett. 16 (1) (2024) 110.

[22] Y. Xiong, L. Chen, P. Liu, T. Yu, C. Lin, C. Yan, Y. Hu, W. Zhou, Y. Sun, A.C. Panayi, F. Cao, H. Xue, L. Hu, Z. Lin, X. Xie, X. Xiao, Q. Feng, B. Mi, G. Liu, All-in-One:

multifunctional hydrogel accelerates oxidative diabetic wound healing through timed-release of exosome and fibroblast growth factor, Small 18 (1) (2022) e2104229.

[23] R. Yu, Y. Yuan, Z. Liu, L. Liu, Z. Xu, Y. Zhao, C. Jia, P. Zhang, H. Li, Y. Liu, Y. Wang, W. Li, L. Nie, X. Sun, Y. Li, B. Liu, H. Liu, Selenomethionine against titanium particle-induced osteolysis by regulating the ROS-dependent NLRP3 inflammasome activation via the β-catenin signaling pathway, Front. Immunol. 14 (2023) 1171150.

[24] K.D. Patel, Z. Keskin-Erdogan, P. Sawadkar, N.S.A. Nik Sharifulden, M.R. Shannon, M. Patel, L.B. Silva, R. Patel, D.Y.S. Chau, J.C. Knowles, A.W. Perriman, H.W. Kim, Oxidative stress modulating nanomaterials and their biochemical roles in nanomedicine, Nanoscale Horiz 9 (10) (2024) 1630–1682.

[25] H. Yang, D. Lv, S. Qu, H. Xu, S. Li, Z. Wang, X. Cao, Y. Rong, X. Li, H. Wu, Y. Chen, J. Zhu, B. Tang, Z. Hu, A ROS-responsive lipid nanoparticles release multifunctional hydrogel based on microenvironment regulation promotes infected diabetic wound healing, Adv. Sci. (2024) e2403219.

[26] Y. Xu, Q. Hu, Z. Wei, Y. Ou, Y. Cao, H. Zhou, M. Wang, K. Yu, B. Liang, Advanced polymer hydrogels that promote diabetic ulcer healing: mechanisms, classifications, and medical applications, Biomater. Res. 27 (1) (2023) 36.

[27] Y. Wu, Y. Wang, L. Long, C. Hu, Q. Kong, Y. Wang, A spatiotemporal release platform based on pH/ROS stimuli-responsive hydrogel in wound repairing, J. Contr. Release 341 (2022) 147–165.

[28] Z. Wang, P. Zhang, Y. Zhao, F. Yu, S. Wang, K. Liu, X. Cheng, J. Shi, Q. He, Y. Xia, L. Cheng, Scutellarin protects against mitochondrial reactive oxygen species-dependent NLRP3 inflammasome activation to attenuate intervertebral disc degeneration, Front. Bioeng. Biotechnol. 10 (2022) 883118.

[29] Y. Tang, L. Liu, R. Jie, Y. Tang, X. Zhao, M. Xu, M. Chen, Negative pressure wound therapy promotes wound healing of diabetic foot ulcers by up-regulating PRDX2 in wound margin tissue, Sci. Rep. 13 (1) (2023) 16192.

[30] A.J. Boulton, L. Vileikyte, G. Ragnarson-Tennvall, J. Apelqvist, The global burden of diabetic foot disease, Lancet 366 (9498) (2005) 1719–1724.

[31] S.A. Hyun, Y.J. Lee, S. Jang, M.Y. Ko, C.Y. Lee, Y.W. Cho, Y.E. Yun, B.S. Lee, J. W. Seo, K.S. Moon, M. Ka, Adipose stem cell-derived extracellular vesicles ameliorates corticosterone-induced apoptosis in the cortical neurons via inhibition of ER stress, Stem Cell Res. Ther. 13 (1) (2022) 110.

[32] C.B. Madelaire, D.P. Silva, S.C.M. Titon, F. Lamadrid-Feris, F.R. Floreste, B. Titon Jr., F.R. Gomes, Contrasting effects of transdermal and implant corticosterone treatments in the American bullfrog wound healing, Philos. Trans. R. Soc. Lond. B Biol. Sci. 378 (1882) (2023) 20220119.

[33] P.B. Milan, N. Lotfibakhshaiesh, M.T. Joghataie, J. Ai, A. Pazouki, D.L. Kaplan, S. Kargozar, N. Amini, M.R. Hamblin, M. Mozafari, A. Samadikuchaksaraei, Accelerated wound healing in a diabetic rat model using decellularized dermal matrix and human umbilical cord perivascular cells, Acta Biomater. 45 (2016) 234–246.

[34] A. Couturier, C. Calissi, J.L. Cracowski, D. Sigaudo-Roussel, C. Khouri, M. Roustit, Mouse models of diabetes-related ulcers: a systematic review and network meta-analysis, EBioMedicine 98 (2023) 104856.

[35] D.G. Armstrong, A.J.M. Boulton, S.A. Bus, Diabetic foot ulcers and their recurrence, N. Engl. J. Med. 376 (24) (2017) 2367–2375.

[36] N. Chaudhari, A.D. Findlay, A.W. Stevenson, T.D. Clemons, Y. Yao, A. Joshi, S. Sayyar, G. Wallace, S. Rea, P. Toshniwal, Z. Deng, P.E. Melton, N. Hortin, K. S. Iyer, W. Jarolimek, F.M. Wood, M.W. Fear, Topical application of an irreversible small molecule inhibitor of lysyl oxidases ameliorates skin scarring and fibrosis, Nat. Commun. 13 (1) (2022) 5555.

[37] Y. Chen, X. Wang, S. Tao, Q. Wang, P.Q. Ma, Z.B. Li, Y.L. Wu, D.W. Li, Research advances in smart responsive-hydrogel dressings with potential clinical diabetic wound healing properties, Mil Med Res 10 (1) (2023) 37.

[38] S. Chen, Y. Zhu, Q. Xu, Q. Jiang, D. Chen, T. Chen, X. Xu, Z. Jin, Q. He, Photocatalytic glucose depletion and hydrogen generation for diabetic wound healing, Nat. Commun. 13 (1) (2022) 5684.

[39] A.P. Veith, K. Henderson, A. Spencer, A.D. Sligar, A.B. Baker, Therapeutic strategies for enhancing angiogenesis in wound healing, Adv. Drug Deliv. Rev. 146 (2019) 97–125.

[40] Y. Liang, M. Li, Y. Yang, L. Qiao, H. Xu, B. Guo, pH/glucose dual responsive metformin release hydrogel dressings with adhesion and self-healing via dual-dynamic bonding for athletic diabetic foot wound healing, ACS Nano 16 (2) (2022) 3194–3207.

[41] S. Rahati, M. Kamalinezhad, A. Ebrahimi, M. Eshraghian, H. Pishva, Accelerated wound healing induced by spinach extract in experimental model diabetic rats with streptozotocin, Sci. Rep. 13 (1) (2023) 14933.

[42] Y. Shou, Z. Le, H.S. Cheng, Q. Liu, Y.Z. Ng, D.L. Becker, X. Li, L. Liu, C. Xue, N.J. Y. Yeo, R. Tan, J. Low, A.R.K. Kumar, K.Z. Wu, H. Li, C. Cheung, C.T. Lim, N.S. Tan, Y. Chen, Z. Liu, A. Tay, Mechano-activated cell therapy for accelerated diabetic wound healing, Adv. Mater. 35 (47) (2023) e2304638.

[43] C. Chai, P. Zhang, L. Ma, Q. Fan, Z. Liu, X. Cheng, Y. Zhao, W. Li, J. Hao, Regenerative antibacterial hydrogels from medicinal molecule for diabetic wound repair, Bioact. Mater. 25 (2023) 541–554.

[44] A.G. Kurian, N. Mandakhbayar, R.K. Singh, J.H. Lee, H.W. Kim, Multifunctional molybdenum-based nanoclusters engineered gelatin methacryloyl as in situ photo-cross-linkable hybrid hydrogel dressings for enhanced wound healing, ACS Appl. Mater. Interfaces 16 (27) (2024) 34641–34655.

[45] J. Chen, Y. Liu, G. Cheng, J. Guo, S. Du, J. Qiu, C. Wang, C. Li, X. Yang, T. Chen, Z. Chen, Tailored hydrogel delivering niobium carbide boosts ROS-scavenging and antimicrobial activities for diabetic wound healing, Small 18 (27) (2022) e2201300.

[46] H. Chen, Y. Guo, Z. Zhang, W. Mao, C. Shen, W. Xiong, Y. Yao, X. Zhao, Y. Hu, Z. Zou, J. Wu, Symbiotic algae-bacteria dressing for producing hydrogen to accelerate diabetic wound healing, Nano Lett. 22 (1) (2022) 229–237.

[47] A.S. Carlini, W. Choi, N.C. McCallum, N.C. Gianneschi, pH-responsive charge-conversion progelator peptides, Adv. Funct. Mater. 31 (13) (2021).

[48] Y. Cai, K. Chen, C. Liu, X. Qu, Harnessing strategies for enhancing diabetic wound healing from the perspective of spatial inflammation patterns, Bioact. Mater. 28 (2023) 243–254.

[49] F. Broglio, M. Papotti, G. Muccioli, E. Ghigo, Brain-gut communication: cortistatin, somatostatin and ghrelin, Trends Endocrinol. Metabol. 18 (6) (2007) 246–251.

[50] S. Werner, R. Grose, Regulation of wound healing by growth factors and cytokines, Physiol. Rev. 83 (3) (2003) 835–870.

[51] S. Knoedler, L. Knoedler, M. Kauke-Navarro, Y. Rinkevich, G. Hundeshagen, L. Harhaus, U. Kneser, B. Pomahac, D.P. Orgill, A.C. Panayi, Regulatory T cells in skin regeneration and wound healing, Mil Med Res 10 (1) (2023) 49.